

RESEARCH

Open Access



Lung infection by *Pseudomonas aeruginosa* induces neuroinflammation and blood–brain barrier dysfunction in mice

Nuria Villalba¹, Yonggang Ma¹, Sarah A. Gahan¹, Aurelie Joly-Amado¹, Sam Spence¹, Xiaoyuan Yang¹, Kevin R. Nash¹ and Sarah Y. Yuan^{1,2*}

Abstract

Background Severe lung infection can lead to brain dysfunction and neurobehavioral disorders. The mechanisms that regulate the lung-brain axis of inflammatory response to respiratory infection are incompletely understood. This study examined the effects of lung infection causing systemic and neuroinflammation as a potential mechanism contributing to blood–brain barrier (BBB) leakage and behavioral impairment.

Methods Lung infection in mice was induced by instilling *Pseudomonas aeruginosa* (PA) intratracheally. We determined bacterial colonization in tissue, microvascular leakage, expression of cytokines and leukocyte infiltration into the brain.

Results Lung infection caused alveolar-capillary barrier injury as indicated by leakage of plasma proteins across pulmonary microvessels and histopathological characteristics of pulmonary edema (alveolar wall thickening, microvessel congestion, and neutrophil infiltration). PA also caused significant BBB dysfunction characterized by leakage of different sized molecules across cerebral microvessels and a decreased expression of cell–cell junctions (VE-cadherin, claudin-5) in the brain. BBB leakage peaked at 24 h and lasted for 7 days post-inoculation. Additionally, mice with lung infection displayed hyperlocomotion and anxiety-like behaviors. To test whether cerebral dysfunction was caused by PA directly or indirectly, we measured bacterial load in multiple organs. While PA loads were detected in the lungs up to 7 days post-inoculation, bacteria were not detected in the brain as evidenced by negative cerebral spinal fluid (CSF) cultures and lack of distribution in different brain regions or isolated cerebral microvessels. However, mice with PA lung infection demonstrated increased mRNA expression in the brain of pro-inflammatory cytokines (IL-1 β , IL-6, and TNF- α), chemokines (CXCL-1, CXCL-2) and adhesion molecules (VCAM-1 and ICAM-1) along with CD11b⁺CD45⁺ cell recruitment, corresponding to their increased blood levels of white cells (polymorphonuclear cells) and cytokines. To confirm the direct effect of cytokines on endothelial permeability, we measured cell–cell adhesive barrier resistance and junction morphology in mouse brain microvascular endothelial cell monolayers, where administration of IL-1 β induced a significant reduction of barrier function coupled with tight junction (TJ) and adherens junction (AJ) diffusion and disorganization. Combined treatment with IL-1 β and TNF α augmented the barrier injury.

Conclusions Lung bacterial infection is associated with BBB disruption and behavioral changes, which are mediated by systemic cytokine release.

*Correspondence:

Sarah Y. Yuan
syuan@usf.edu

Full list of author information is available at the end of the article



© The Author(s) 2023. **Open Access** This article is licensed under a Creative Commons Attribution 4.0 International License, which permits use, sharing, adaptation, distribution and reproduction in any medium or format, as long as you give appropriate credit to the original author(s) and the source, provide a link to the Creative Commons licence, and indicate if changes were made. The images or other third party material in this article are included in the article's Creative Commons licence, unless indicated otherwise in a credit line to the material. If material is not included in the article's Creative Commons licence and your intended use is not permitted by statutory regulation or exceeds the permitted use, you will need to obtain permission directly from the copyright holder. To view a copy of this licence, visit <http://creativecommons.org/licenses/by/4.0/>. The Creative Commons Public Domain Dedication waiver (<http://creativecommons.org/publicdomain/zero/1.0/>) applies to the data made available in this article, unless otherwise stated in a credit line to the data.

Keywords Blood–brain barrier, Lung infection, Permeability

Introduction

Severe lung injury caused by bacterial infections may contribute to clinical complications such as multiple organ dysfunction, including cerebral and neurological disorders, which have been associated with high morbidity and mortality [1–3]. Several factors, from pathogen load to duration of infection, determine patients' outcome with neuroinflammation as the link between long-term neurological damage and brain dysfunction resulting in a myriad of cognitive complications and behavioral symptoms.

The importance of lung-brain communication has been recognized based on strong clinical and experimental evidence. For example, clinical studies have demonstrated that patients with pneumonia often experience changes in mental status, such as confusion, low alertness and even delirium, specifically in older patients [4]. Additionally, community-acquired pneumonia, the most prevalent cause of sepsis, can also induce acute and chronic changes in the central nervous system (CNS) [5–8]. Sepsis-associated encephalopathy (SAE), a well-characterized state of long-term cognitive impairment and neurological dysfunction develops in approximately 70% of sepsis survivors [9]. The causes of SAE are not completely understood albeit one of the explanations could be that a compromised BBB leads to brain dysfunction and CNS pathology [10, 11]. A broad range of pathogens are capable of permanently or temporarily affect brain functions [12, 13]. Unlike viruses, which can infiltrate the CNS, direct dissemination of bacteria into the brain is rare and, therefore, other factors must contribute to the cerebral pathophysiology.

In the present study, we used a clinically relevant mouse model of bacterial pneumonia. We inoculated freshly prepared PA intratracheally into mice and examined the relationship between lung infection and cerebral dysfunction. Specifically, we tested whether the changes in the brain are due to a direct effect of bacteria penetrated the CNS, or indirectly via systemic and neuroinflammation triggered by pulmonary infection.

Methods

Bacteria growth and inoculum preparation

PA was selected for this study because it is known to be the most common cause of nosocomial pneumonia [14]. PA (PAO1 strain) (ATCC; #27853) was cultured following manufacturer's instructions. Prior to infection, freshly cultured bacteria from frozen aliquots

(– 80 °C) were grown overnight at 37 °C in tryptic soy broth (Remel; #R455052) with vigorous agitation (180 rpm) and harvested in log phase to an optical density at 600-nm (OD_{600}) of 0.3 (only for survival studies, mice were inoculated with $OD_{600}=0.6$). Bacteria were centrifuged at 3000 rpm for 10 min, rinsed and resuspended in sterile phosphate-buffered saline (PBS, pH 7.4). Serial dilutions and colony count of the inoculum were performed to obtain the number of colony-forming units (CFUs) per mL (CFU/mL). For histology experiments and multiphoton imaging, PA labelled with a green fluorescent protein gene (PA-GFP; ATCC; #10145GFP) was used. PA-GFP was cultured in nutrient agar (BD Difco™; #213000) or broth (BD Difco™; #234000) supplemented with 300 µg ampicillin following manufacturer's instructions as described above and then inoculated into mice.

Animal model of pneumonia

Male and female C57BL/6 mice between 8 and 16 weeks of age were used in all experiments. All mice were housed in a temperature and humidity-controlled housing with a 12-h light:dark diurnal cycle. Littermates of the same age were allocated to experimental groups. All experimental animal protocols were approved by the University of South Florida Institutional Animal Care and Use Committee (IACUC; protocol 8421R) and were conducted in accordance with the Guide for Care and Use of Laboratory Animals.

Under anesthesia, forty-microliters of bacteria reconstituted in sterile PBS [$OD_{600}=0.3$; 2×10^7 (CFUs/mL)] were directly injected into the mouse lungs by intratracheal instillation using a 22-G cannula via the oropharynx using a mouse intubation kit (Hallowell EMC, MA) and an otoscope. Control group received the same volume of sterile PBS (uninfected group). After inoculation, mice were kept in a supine position for a few breaths or at least 30 s. Once awake, mice were returned to their cages, monitored regularly and allowed access to food and water. For clinical relevance, antibiotics (imipenem + cilastatin formulated in 0.9% saline solution) were administered subcutaneously at a dose of 5 mg/Kg starting at 6 h post-infection. The general conditions of each mouse were monitored over a period of 7 days. All procedures were performed in a bio-safety cabinet in a designated bio-safety level-II room according to the Biosafety protocols approved by the University of South Florida.

Measurement of microvascular permeability in vivo

The leakage of circulating solutes across microvessels was evaluated by measuring tissue (brain and lung) accumulation of tracer molecules of different sizes using the ratiometric assay and near-infrared imaging (NIR) as we previously described [15]. Time-course of vascular permeability changes was assessed in anesthetized mice intravenously injected through the retro-orbital venous sinus with sodium fluorescein (NaFl; 5 μ L/g of a 100 mg/mL NaFl solution; 376 Da; Sigma-Aldrich; #6377) at 24 h, 7 days and 1-month post-infection; this timeline represents a spectrum of time ranging from the acute infectious period (24 h) to the long-term effects (1 month). Then, mice were anesthetized with urethane (1.75 mg/Kg; intraperitoneally) and transcardially perfused with ice-cold 0.1 M PBS. After dissection, brains and lung lobes were harvested, weighed and homogenized. Tissue homogenates were centrifuged at 12,000 \times g for 20 min at 4 °C. The fluorescence of a 100 μ L aliquot of the brain and lung samples along with 100 μ L of blank or standards was measured on a fluorescence microplate reader (SpectraMax M3; Molecular Devices, Sunnyvale, CA). The concentrations of the samples were within the linear range of the standard curve. Amount of dye (ng) was normalized per pg or μ g protein in the extract.

In a different set of experiments, permeability to Alexa Fluor 70-kDa (5 μ g/g of a 1 mg/mL solution; Sigma-Aldrich; #R9379) was assessed in the lungs of controls and infected animals at 24 h post-infection. For NIR of lungs (left lobe), animals received albumin (Albumin-CF[®]680 dye; ~ 70-kDa; 5 μ g/g of a 1 mg/mL solution; Biotium; #20292). Tracer was allowed to distribute in freely moving mice for 4 h and then animals were cardially perfused with PBS. For NIR imaging of brains, anesthetized animals received a combined injection of 10-kDa dextran (10 μ g/g of a 1 mg/mL solution; CF[™]790-10-kDa dextran; Biotium; #80121) and albumin (Albumin-CF[®]680 dye) intravenously. Organs (left lung lobe and whole brain) were imaged at 700 and 800 nm with a near-infrared imaging system (Odyssey CLx; LI-COR Biosciences, Lincoln, NE).

Measurements of bacteria load in tissues and CSF

Bacterial load in mouse lungs and spleen were performed at different time points after infection. Tissues were weighted and then homogenized in tryptic soy broth under sterile conditions. One hundred μ L of the homogenate were plated on tryptic soy agar plates for quantification of colonies. For quantification of bacterial load in the brain, CSF samples were obtained under anesthesia through the cisterna magna using a custom-made glass cannula. Ten-fold serial dilutions of the homogenates and

CSF were prepared and spread onto agar plates. Next day, CFUs were counted. For the identification of bacteremia (qualitatively), 100 μ L of blood were obtained under sterile conditions and cultured in culture vials (BD Bactec[™] peds plus culture vials; #442020) for 4 days. Then, 100 μ L of the culture vials were streaked onto a 5% sheep blood in tryptic soy agar plates (Hardy diagnostics; #A10) for colony counts.

Proinflammatory mediators in plasma and brain tissue

Plasma samples (diluted 1:2) obtained from blood collected by cardiac puncture in heparin tubes (BD Microtainer[®] blood collection tubes; BD Biosciences; #365965) were analyzed for IL-6, IL-1 β and TNF- α using indirect sandwich enzyme-linked immunosorbent assay (ELISA) (Sigma-Aldrich; #RAB0308 and #RAB0477) according to the manufacturer's instructions.

Total RNA was extracted from brain cortices and hippocampi from PA-infected and control animals using TRIzol[®] Reagent (Invitrogen; #15596) and RNeasy Plus kit (Qiagen). RNA concentration was measured using NanoDrop One Spectrophotometer (Thermo scientific). Reverse transcription (RT)-PCR of RNA was performed using High-Capacity RNA-to-cDNA Kit (Thermo Fisher Scientific; #4387406). cDNA was amplified for real-time detection with TaqMan[™] Gene Expression Master Mix (Thermo Fisher Scientific; #4369016) plus individual primers for IL-1 β , IL-6, TNF- α , ICAM-1, VCAM-1, CXCL1 and CXCL2 (FAM tagged; Thermo Fisher Scientific) on a Biorad CFX Connect[™] machine. Expression data were normalized to Gapdh mRNA levels. The data were calculated as $2^{[Ct(\text{Gapdh}-\text{gene of interest})]}$ to compare infected group to controls. MIQE guidelines were followed for all the PCR experiments and analysis [16].

Flow cytometry

Mice were euthanized and perfused with sterile PBS through the left ventricle of the heart. The brains (400–500 mg; without the cerebellum) were harvested, cut along the coronal plane with a razor into three pieces and digested into cell suspensions using a Multi Tissue Dissociation kit 1 (Miltenyi Biotec, Germany; #130-110-201) and a gentleMACS[™] OctoDissociator with heaters (Miltenyi Biotec; #130-096-427) following manufacturer's instructions. During the final steps, myelin and erythrocytes were removed using a neural debris removal kit (Miltenyi Biotec; #130-109-398) and red cell lysis solution (Biolegend; #420301), respectively. Total cell count in each brain was quantified using a Luna-II automated cell counter. Cells were then subjected to antibody staining for flow cytometry analysis. The cell suspension was stained with a panel of antibodies against CD45-Alexa 700 (1:1200; Biolegend; #147716) and CD11b-PE dazzle

(1:800; Biolegend; #101256). A corresponding isotype IgG antibody was used as negative staining control. Dead cells were excluded using the live/dead stain Zombie NIR fixable viability dye (1:2000; Biolegend; #423105). The samples were run on a Cytex[®] Northern Lights[™] cytometer (Cytex biosciences) and data were analyzed using FlowJo (FlowJo LLC, Ashland, OR). Cell populations were calculated based on relative abundance obtained by flow cytometry (number = total cell count × % of positive cells) [17]. Cells were gated using FSCA and FSCH to identify singlets, then gated for live cells by taking a population that was negative for live/dead stain. Antibodies concentrations were chosen based on previous antibody titrations to determine the dilution that provides the best separation of cell populations. Each “*n*” refers to a single brain obtained from a single mouse, so that each *n* represents a different mouse. Brains were not pooled together for these experiments. See Additional file 1: Fig. S1 for gating strategy used.

Endothelial cell culture

Primary mouse brain microvascular endothelial cells (Cell Biologics, Chicago, IL; #C57-6023) were grown in the recommended culture medium (Cell Biologics; #M1168) supplemented with 10% (v/v) fetal calf serum at 37 °C and 5% CO₂, split at a ratio of 1:2 and used at passage two. Endothelial cell monolayers were used for barrier integrity and immunofluorescence experiments.

Assessment of barrier function by electric cell-substrate impedance sensing (ECIS) assay

Barrier integrity of brain microvascular endothelial cells was performed using a protocol previously described by our group [15, 18]. Cell monolayers were grown to reach confluence in order to obtain a polarized endothelium as evidenced by high and stable transendothelial electrical resistance (TER, ohm) values [15]. Mouse brain endothelial cell barrier function was determined by measuring the cell–cell adhesion barrier resistance to electric current using an ECIS system (Model ZΘ; Applied Biophysics Inc., Troy, NY). Briefly, 250 μL of cell suspension (5 Å ~ 105 cells per mL) were seeded to each well of two ECIS culture arrays consisting of 8-wells with 10-gold microelectrodes (8W1E+) following manufacturer’s instructions. Resistance was recorded in real time with the following settings: alternating current (1-V) and 4-kHz frequency at 7-s intervals. Data were normalized to baseline measurements just prior to the onset of treatment (*t*=0) and expressed as resistance change (ohms). Both data acquisition and processing were performed using the ECIS Z-theta Analysis Software supplied by Applied Biophysics to determine the resistance (ohm @ 4 kHz) values reflecting cell monolayer integrity and

overall response to cytokines. In a different set of experiments, cells were exposed to IL-1β (Miltenyi Biotec; #130-094-053) and IL-1β + TNF-α (Biolegend; #575204). Cytokines were dissolved in PBS + 0.1% BSA at 2, 20 and 200 ng/mL. Vehicle control was diluent alone at the same volume as treatment. Data were normalized to baseline, and comparisons were made between cytokine treatment and vehicle control. Data show mean ± S.E.M. (*n* = 3).

Immunocytochemistry

Brain endothelial cell monolayers were plated on Lab-Tek[®] chamber slides (ThermoFisher Scientific; #1777399PK) and exposed to cytokines (IL-1β, 20 ng/mL), washed in PBS containing 2 mM CaCl₂ and 2 mM MgCl₂ and then fixed in 2% paraformaldehyde (PFA) in PBS for 5 min followed by 4% PFA for 15 min. Cells were washed in PBS twice, permeabilized and blocked (in 0.3% Triton-X and 10% normal donkey serum in 3% BSA/PBS) for 1 h at room temperature. Slides were incubated with the primary antibodies: zona occludens-1 (ZO-1; 1:100; ThermoFisher; #40-2200), claudin-5 (1:50; ThermoFisher, #35-2500) and VE-cadherin (1:1000; Abcam; ab205336) overnight at 4 °C. Next day, slide chambers were washed seven times with 3% BSA/PBS and incubated with appropriate secondary Alexa Fluor[®] antibodies (Invitrogen; diluted at 1:500). Chambers were carefully removed, and slides were then cover slipped using ProLong[™] diamond antifade mountant with DAPI (Life Technologies; #P36966).

Tissue processing and histology

Tissues (brain and lung) harvested from animals 24 h after infection with GFP-labelled PA were subjected to multiphoton imaging. Mice were anesthetized and injected intravenously with 200 μL of Evans blue solution containing 3% Evans blue fluorescent dye (Sigma-Aldrich; #E2129) in 5% BSA/PBS to visualize vasculature prior to organ extraction and ex-vivo multiphoton imaging.

For visualizing PA distribution in tissue by confocal microscopy, mice infected with GFP-labelled PA and controls were anesthetized and intracardially perfused through the left ventricle with PBS and 4% PFA thereafter. Organs (lungs, spleen and brains) were post-fixed in 4% PFA overnight, rinsed and preserved in 10% sucrose solution in PBS for one day or until the tissue sank to the bottom. Mouse tissues were collected and embedded in Tissue Plus[®] O.C.T. compound (Fisher HealthCare; #4585) in disposable base molds (Fisher HealthCare; #22363553). Blocks were then frozen in liquid nitrogen and stored in – 80 °C until sectioned in a cryostat. Frozen blocks were cut into section (15 μm thick) on a Leica CM1950 cryostat and slides were stored at – 20 °C until use. On the day of the experiment, slides were thawed in

the hood overnight and stained with Dylight 488-conjugated *Lycopersicum esculentum* lectin (1:100; Vector laboratories, Burlingame, CA; #DL-1174) to visualize brain microvessels. Slides were mounted in ProLong™ diamond antifade mountant with DAPI.

Brain microvessels from control and PA-infected mice were freshly isolated from brain cortices as previously described [19]. Briefly, pial vessels were carefully removed, and the remaining tissue was homogenized with a loose-fitting Dounce homogenizer in MCDB 131 medium. Homogenates were then centrifuged for 5 min at 2000 g at 4 °C. Pellets were resuspended in 15% (wt/vol) dextran-PBS and centrifuged again at 10,000 g for 15 min at 4 °C. Myelin was carefully removed from the tube and the pellet was removed with 1 mL DPBS and passed through a 40 µm strainer. The strainer was reversed and washed with 10 mL MCDB 131 media to retrieve the microvessels. Microvessels were fixed in 2% PFA and cytospinned onto microscope slides.

For leukocyte infiltration into the tissue, lung and brain slides were permeabilized and blocked for 1 h at room temperature in 10% normal donkey serum diluted with PBS/3% BSA and 0.3% Triton-X. Slides were incubated overnight with the primary antibodies against neutrophils for the lung (1:100; Cederlane; #CL8993AP) or CD45 for the brain (1:100; Cell Signaling; #70257) overnight at 4 °C. Next day, slides were washed seven times with 3% BSA/PBS and incubated with appropriate secondary Alexa Fluor® antibodies (Invitrogen; diluted at 1:500). Slides were then cover slipped using ProLong™ diamond antifade mountant with DAPI. All antibody dilutions used were optimized by titration.

For visualizing lung structure hematoxylin and eosin (H&E) staining was performed. Animals were transcardially perfused via the left ventricle with PBS first and then 4% PFA. After one day of post-fixation in the same fixative, lungs were embedded in paraffin using an automatic tissue processor (Thermo Scientific) and then sectioned (4 µm) using a microtome. Slides were deparaffinated and then stained with H&E following standard procedures. All slides were imaged at the same time and using the same settings with a brightfield Olympus VS120 slide scanning imaging system (×20 objective).

Immunofluorescence of TJ and AJs

Anesthetized mice were transcardially perfused through the left ventricle with ice-cold PBS. Mouse brains were dissected, embedded in Tissue-Tek® O.C.T. compound (Sakura Finetek USA Inc., Torrance, CA) and snap-frozen ("fresh frozen tissue"). Coronal sections were sectioned at 15 µm on a cryostat and stored at -80 °C until use. Cryosections were thawed and immediately fixed in either ice-cold methanol (claudin-5) or 4% PFA (VE-cadherin) for

15 min and then rinsed in PBS twice. Mouse brain sections were permeabilized and blocked for 1 h at room temperature in blocking buffer (0.3% Triton X-100 and 10% normal goat serum in 3% BSA/PBS) and incubated overnight at 4 °C with the following primary antibodies: claudin-5 (1:50; Thermofisher; #35-2500), VE-cadherin/CD144 (1:100; BD Pharmingen; #555289) diluted in blocking buffer at constant agitation. To visualize brain microvessels, sections were incubated with Dylight 488-conjugated *Lycopersicum esculentum* lectin (1:100; Vector laboratories; #DL-1174) during the primary antibody incubation. After the washing steps, sections were incubated with fluorescent secondary Alexa Fluor antibodies (Invitrogen; 1:500) for 1 h at room temperature. Coronal brain sections were washed for 1 h, mounted in ProLong™ diamond antifade mountant with DAPI (Life Technologies; #P36966) and imaged using a Leica DMi8 STED confocal microscope using a 20×HC PLAPO, N.A. 0.75 objective (Leica Microsystems, Rueil-Malmaison, France).

Western blotting

Brain homogenates were run on a 4–20% Tris–Glycine gel (Mini-protean TGX gel; Bio-Rad laboratories; #4561094) and transferred onto a nitrocellulose membrane (TransBlot® Turbo RTA mini nitrocellulose transfer kit; Bio-Rad laboratories; #1704270). The membranes were blocked in intercept blocking buffer (Li-Cor; #927-70001) for 1 h at room temperature, probed with primary antibodies against claudin-5 (1:250; Cell Signaling technology; #49564), occludin (1:500; BD Biosciences; #611091), VE-cadherin (1:1000; Abcam; ab205336), GFAP (1:1000; Sigma-Millipore; MAB360), and beta-actin (1:1000; Li-Cor; #926-42212 and #926-42210) diluted in intercept antibody diluent buffer (Li-Cor; #927-75001). Membranes were washed with PBS-T (0.1% Tween-20) and probed with Li-Cor IRDye secondary antibodies diluted in intercept antibody diluent buffer for 1 h at room temperature. The washed membranes were then imaged on a Li-Cor Odyssey CLx imaging system and blots were analyzed using the Image Studio Lite 5.2.5 software. Relative protein abundance was obtained by densitometry analysis. The signal intensity of all protein bands was normalized to the beta-actin loading control band (relative abundance).

Microscopy and imaging

Confocal microscopy was performed using two different lenses ×20 HC PL APO (0.75NA [numerical aperture], WD [working distance] 0.62 mm) and a ×63 HC PL APO (Oil immersion, 1.4NA, WD 0.14 mm). For confocal microscopy, GFP-labelled PA was excited with the 488-nm laser.

Two-photon imaging was performed using an Olympus FV1000 MPE microscope equipped with 4 spectral detectors, a $\times 25$ XL Plan N 1.05 N.A. water immersion objective and a Coherent Chameleon Ultra II IR laser. For multiphoton imaging, GFP-labelled PA was excited with 924-nm laser pulses, emission was detected at 500–520 nm. Evans blue was excited at 945-nm and detected at 620–750-nm. The raw 3D images were reconstructed from z-stacks using Imaris software 9.7 (RRID:SCR_007370).

Open field behavioral test

Spontaneous locomotor activity and anxiety-like behavior were measured by open field test assessed at 1-week after PA infection [20]. Mice were placed in an open field chamber and were allowed free exploration for 15 min. The distance traveled was recorded and analyzed using ANY-maze[®] video tracking system (Stoelting Co, IL, USA). Increased overall distance travelled in the chamber and time spent in the center were considered an index of greater locomotor activity and anxiety-like behavior.

Hematology and biochemistry

White blood cell counts, cell differentials (neutrophils and monocytes) and total protein were measured in mouse blood collected in heparin tubes using a ProCytex Dx hematology analyzer (IDEXX, Westbrook, Maine). Blood pH was measured in fresh blood using an iSTAT device (Abbott, Hightstown, New Jersey).

Statistical analysis

Data were analyzed using GraphPad Prism (version 9.4.0; GraphPad Software Inc., San Diego, CA). Reported values are expressed as mean \pm standard error of the mean (SEM). For animal experiments, female and male mice were randomly selected and used as biological replicates. Normality of the data was tested using the Shapiro–Wilk test. For data that were not normally distributed (nonparametric data), the Mann–Whitney test (two groups, one variable) or Kruskal–Wallis test followed by Dunn's correction (> 2 variables) was used. Data with normal distribution were analyzed by a two-tailed unpaired Student's *t*-test (one variable) or one-way ANOVA with Dunnett's or Tukey's correction (> 2 variables). Statistical test used to analyze the data is described in the figure legends. In all tests a 95% confidence interval was used. Figures show exact *P* values.

Results

Effect of PA inoculation on mouse mortality and lung injury

PA-induced pneumonia was associated with mouse mortality, which depended on the inoculum's load or number

of infecting bacteria. Survival studies were performed using two inoculum's loads, OD₆₀₀ of 0.3 ($\sim 2 \times 10^7$ CFUs/mL) and OD₆₀₀ of 0.6. Infected mice with PA at an OD₆₀₀ of 0.3 and OD₆₀₀ of 0.6 ($\sim 9 \times 10^8$ CFUs/mL) induced a 16% and 50% mortality at day 7, respectively, compared to 100% survival in the control group (Additional file 2: Fig S2a). All infected mice (OD₆₀₀ 0.3) showed lethargy, hypothermia and remained immobile or moved slowly in the cage starting at 4 h post-infection (Additional file 2: Fig. S2b). Those who did not die within 24 h showed significant signs of improvement in mobility and appearance. Additionally, PA also caused acidosis and high levels of proteins in the blood (hyperproteinemia), both metabolic parameters associated with active infection (Additional file 2: Fig. S2c, d). Together, these data support the validity of the PA-induced pneumonia model.

Next, we assessed the pulmonary vascular barrier in vivo in PA infected mice (OD₆₀₀ 0.3; 24 h post-infection) and uninfected controls by measuring extravasation of intravenously injected 70-kDa fluorescent tracer. Upon PA challenge, plasma leakage from lung microvessels, indicated by higher interstitial accumulation of 70-kDa dextran, was detected in infected mice compared with that in controls (Fig. 1b, c). PA infection also caused a significant albumin leakage in the lungs (Fig. 1d). Lung transvascular albumin flux increased by approximately eightfold, peaked at 6 h post-infection and started to decrease by day 7 post-infection. H&E staining of lung sections post-infection showed that PA evoked a robust inflammatory response (Fig. 1e, f). Compared to control lungs characterized by thin alveolar walls and clear alveolar airspaces with few numbers of neutrophils confined to the septal network (Fig. 1e), lung sections obtained from animals inoculated with PA were characterized by alveolar infiltration of neutrophils (Fig. 1f).

BBB leakage following PA lung infection

Next, we studied whether PA-induced lung infection (OD₆₀₀ 0.3) causes BBB permeability changes. BBB leakage was first evaluated 24 h after infection. We used NIR imaging of whole brains after intravenous administration of 10-kDa and 70-kDa fluorescent tracers (Fig. 2a–d). Significant leakage of both tracers into the brain parenchyma was detected in the infected group. Importantly, paracellular permeability to 10-kDa dye was higher than the 70-kDa, suggesting a size-depending opening of the BBB (Fig. 2a–d). The time-course of BBB permeability changes (“BBB opening and recovery”) was evaluated with NaFl at 24 h, 7 days, and 1-month after infection. Our results indicate a time-dependent increase in the degree of BBB hyperpermeability, which peaked at 24 h after lung infection and decreased by $\sim 80\%$ by 1-month post-infection (Fig. 2e). The disruption of the BBB was

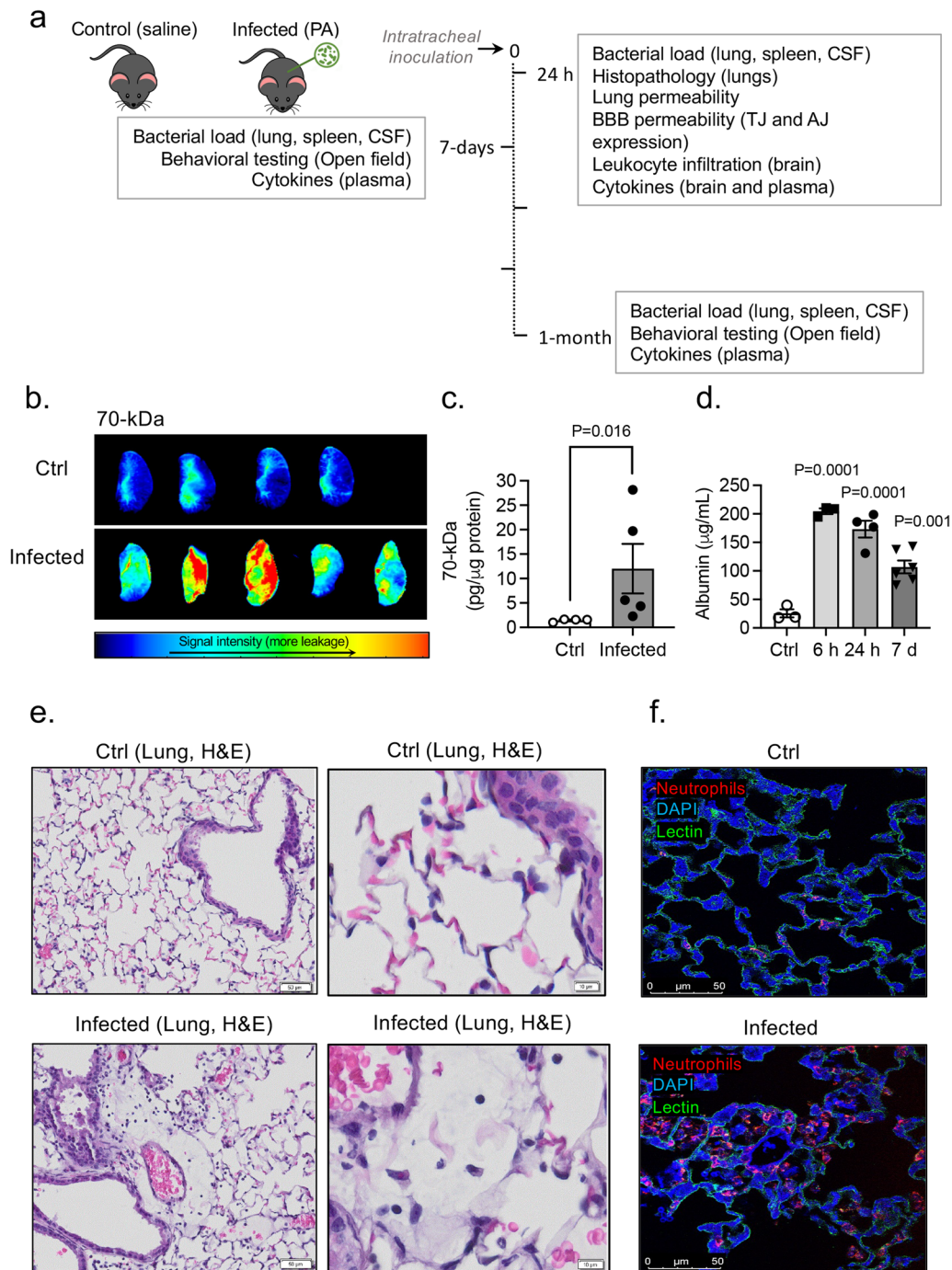


Fig. 1 Effects of PA pneumonia on lung inflammation. **a** Schematic diagram showing experimental design. Animals were exposed to PA on day 0 and then experiments were performed 24 h, 7-days or 1-month post-infection. **b** Representative NIR fluorescence images of the left lung lobe obtained from control and PA infected mice at 24 h post-infection (OD_{600} 0.3) showing the distribution of 70-kDa tracer within the lung tissue. **c** Summary data showing lung permeability of 70-kDa tracer. Mann–Whitney test, $P=0.016$ vs. control (uninfected) group. **d** Plasma leakage indicated by increased levels of albumin in bronchoalveolar lavage fluid (BALF) obtained from control and PA-infected mice at different time points post-infection (6 h, 24 h, and 7 days). Kruskal–Wallis test, $P=0.0001$, $P=0.001$ vs. control (uninfected) group. **e** Histological analysis by conventional H&E staining of lung sections in control and PA-infected mice 24 h post-infection (OD_{600} 0.3). **f** Representative confocal images of neutrophil immunodetection (red), lectin-positive brain endothelial cells (green) and DAPI (nuclei; blue) in the brain from a control (up) and a PA-lung infected mouse 24 h post-infection (bottom). In all graphs, each point indicates data from an individual animal, bar graphs (columns and error bars) show mean \pm S.E.M

associated with changes in mRNA expression of AJs and TJs in the brain at different time points post-infection (Fig. 2f). VE-cadherin mRNA levels decreased by day 7 and remained low 1-month after infection. Claudin-5 mRNA levels decreased at earlier time points (24-h) after infection while occludin mRNA levels remained unchanged. Consistent with BBB breakdown, VE-cadherin and occludin protein levels were significantly reduced in infected animals compared to controls (Fig. 2g; Additional file 3: Fig. S3a). The length of the TJ proteins claudin-5 and the AJ protein VE-cadherin on cortical capillaries of PA-infected mice was reduced as assessed by immunofluorescence confocal microscopy (Fig. 2h).

Lung infection by PA causes anxiety-like behaviors

Next, we assessed both groups of mice for locomotor and anxiety-like behavior in an open field 7 days after saline or PA inoculation (OD_{600} 0.3) (Fig. 3a). PA infection increased the total distance travelled in the open field (Fig. 3b) and decreased the amount of time animals remained immobile (Fig. 3c); the amount of time spent in the brightly-lit center of the open field was higher in infected animals compared to controls (Fig. 3d). The results of the open field test indicate PA-infected animals had increased locomotor activity and anxiety-like behavior preferring to stay in the center of the box compared with uninfected controls.

Tissue distribution of PA in vivo

We next characterized the spread of infection in mice intratracheally inoculated with PA (OD_{600} 0.3) 24 h, 7 days, and 1-month after pseudomonas infection. We examined bacteria load in the organs of infected mice by quantifying CFUs in lung and spleen homogenates and CSF (Fig. 4a). In the lungs, bacterial load decreased by ~fourfold 1-month after infection. PA load was also measured in the spleen, which was used as a peripheral organ to assess whether there is systemic dissemination of PA. In the spleen, PA was detected, although bacterial load was lower compared to lung at all time points post-infection (Fig. 4a). Next, we evaluated the presence of PA

in the brain. We chose CSF for quantification of CFUs over homogenized brain tissue since ~90% of infected animals showed bacteremia 24 h post-inoculation and brains could be contaminated with blood containing bacteria, which could provide misleading results. In parallel to the quantification of bacterial loads, we performed confocal microscopy to visualize GFP-labeled PA distribution within the lungs, spleen and brain. As shown in Fig. 4b, c, 24 h after infection PA was detected with abundance in the lungs, mainly around the airways and spleen. In the brain, we studied three putative sites of entry into the CNS: meningeal vessels, choroid plexus, brain parenchyma, hippocampus and isolated brain microvessels (Fig. 4d–g). We did not detect PA in any of those locations indicating the absence of PA infiltration into the CNS. Next, to confirm the lack of distribution of PA in live tissue, we performed multi-photon microscopy in freshly harvested lungs and brains 24 h post-infection. The 3D reconstruction of z-stacks of brains and lungs confirmed results seen on fixed tissues. In the lungs, PA was localized throughout the lung, while no bacteria were detected in the brain parenchyma or inside brain capillaries (Additional file 4: video 1, Additional file 5: video 2, Additional file 6: video 3, Additional file 7: video 4).

Appearance of leukocytes in the CNS during PA pneumonia

We next investigated the potential systemic effects of PA-induced lung infection. PA inoculation (OD_{600} 0.3) into the lungs caused an increased level of total white blood cell count, along with significantly higher number of neutrophils and monocytes 24 h post-infection (Fig. 5a, b). In addition, we studied whether PA pneumonia triggers an inflammatory response in the brain and evaluated whether there is infiltration of circulating leukocytes into the brain and changes in microglia number. In the CNS parenchyma, we found increased infiltration of leukocytes at 24 h after infection (Fig. 5c, d, f). Using flow cytometry, we quantified subpopulation of leukocytes in brain homogenates according to the expression of CD11b and CD45: microglia ($CD11b^+ CD45^{low}$) and myeloid leukocytes ($CD11b^+ CD45^{hi}$) (for gating strategy see Additional file 1: Fig. S1) [21]. Analysis by flow cytometry

(See figure on next page.)

Fig. 2 Effects of PA lung infection on BBB permeability and cell–cell junction expression. Representative NIR fluorescence images of whole brains obtained from control and PA infected mice (OD_{600} 0.3) showing the distribution of (a) 10-kDa and (c) 70-kDa tracers within the tissue. b, d Summary data showing BBB paracellular permeability of 10-kDa and 70-kDa fluorescence tracers. Mann–Whitney test, $P < 0.05$ vs. control (uninfected) group. e Time course of BBB permeability changes to small size solutes as measured by NaFl uptake starting at 24 h post-infection to 1-month post-infection (OD_{600} 0.3). Kruskal–Wallis test, $P = 0.01$ and $P = 0.0002$ vs. control (uninfected) group. f Summary data showing mRNA expression levels of VE-cadherin, occludin and claudin-5 in brains harvested from control and PA infected mice at 24 h, 7 days and 1 month after infection. Kruskal–Wallis test, $P = 0.01$ and $P = 0.003$ and $P = 0.002$ vs. control (uninfected) group. g VE-cadherin, occludin and claudin-5 immunoblotting in brain homogenates obtained from control and lung infected (24 h) mice, and quantification of their protein abundance relative to β -actin loading control. h Representative confocal images of brain cortex from control and PA-infected (24 h) mice of VE-cadherin and claudin-5 (red) co-stained with lectin (blue, magenta-merged). In all graphs, each point indicates data from an individual animal, bar graphs (columns and error bars) show mean \pm S.E.M

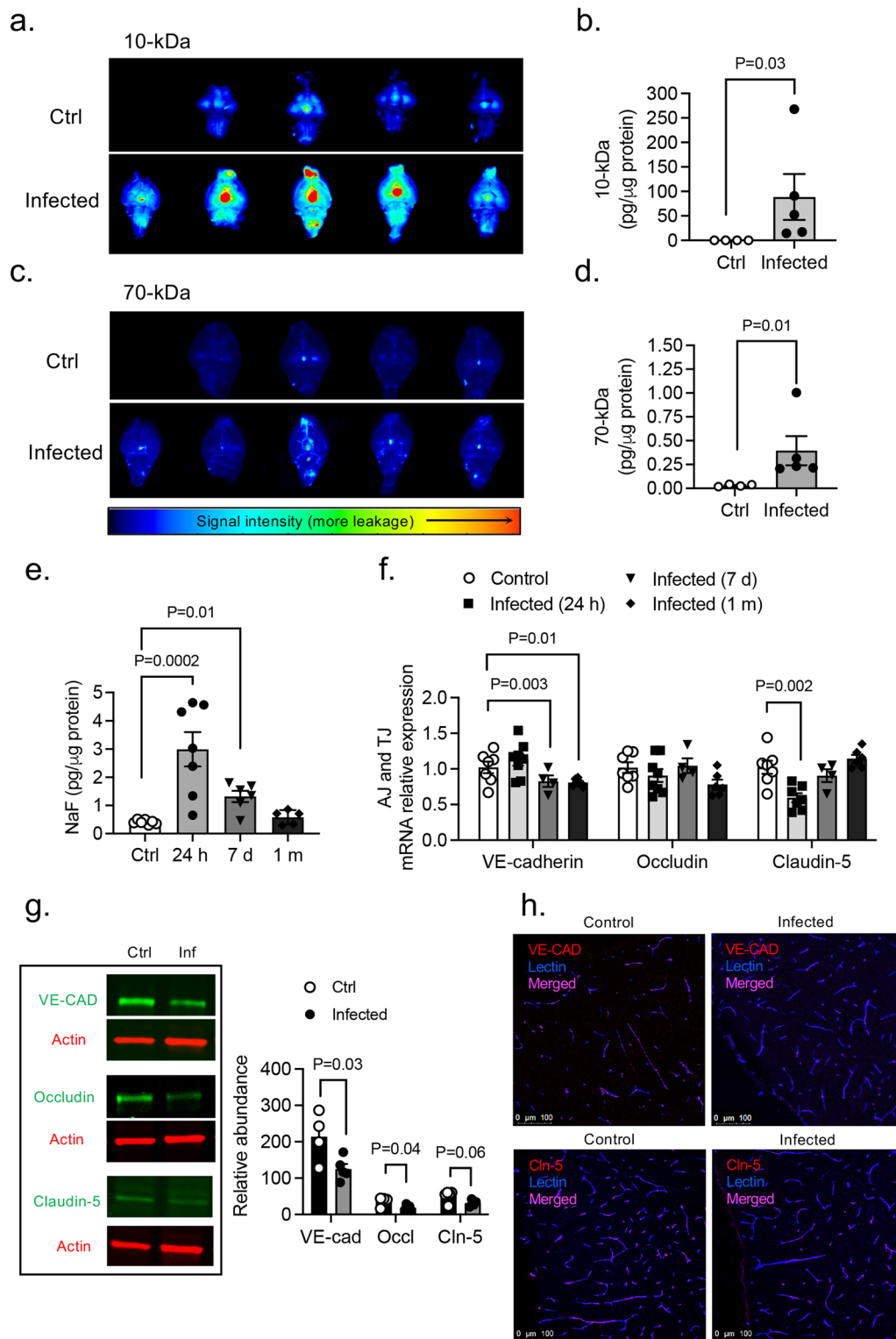


Fig. 2 (See legend on previous page.)

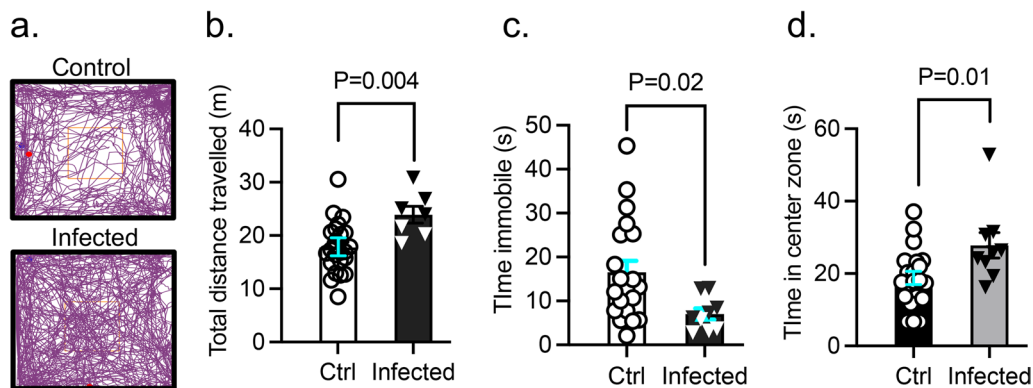


Fig. 3 Effect of PA pneumonia on mouse behavior. **a** Representative tracks of control and PA-infected mice (OD_{600} 0.3) recorded by ANYMaze[®] video system during the open field test. **b** Total distance traveled by control and PA-infected mice. **c** Time mice remained immobile in the open field. **d** Time spent in the center of the open field by controls and PA-infected mice. Mann–Whitney test, $P=0.004$, $P=0.02$, $P=0.01$ vs. control (uninfected) group. In all graphs, each point indicates data from an individual animal, bar graphs (columns and error bars) show mean \pm S.E.M. In all graphs, each point indicates data from an individual animal, bar graphs (columns and error bars) show mean \pm S.E.M

confirmed elevated leukocyte ($CD45^+$) infiltration in the brain 24 h post-infection compared to controls (Fig. 5c, d) which was corroborated by immunofluorescence (Fig. 5f). We observed no changes in the microglia number retrieved from brain tissue (Fig. 5e). GFAP protein expression in mouse brain tissue was increased in the infected group compared to controls (Fig. 5g; Additional file 3: Fig. S3b), which was confirmed by immunofluorescence confocal microscopy (Fig. 5h) indicating reactive astrogliosis.

PA pneumonia upregulates systemic cytokines and causes neuroinflammation

We next measured three representative systemic inflammation-derived proinflammatory cytokines (IL-1 β , IL-6 and TNF- α) following PA administration (OD_{600} 0.3). There was significant elevation of these proinflammatory cytokines in the plasma after lung infection peaking at early time points (6–24 h) (Fig. 6a–c). We also examined the brain's inflammatory state *in vivo* after PA lung infection. Notably, our results showed an upregulated transcriptional expression of cytokines (IL-1 β , IL-6 and TNF- α), adhesion molecules (VCAM-1, ICAM-1) and chemokines (CXCL1 and CXCL2) after infection in both brain cortex (Fig. 6d–f) and hippocampus (Fig. 6g–i).

Cytokine-induced brain endothelial barrier dysfunction

Cytokines are known to regulate not only immunity, but also barrier function [22–25]. Once we determined that PA lung infection increases the level of circulating cytokines and there is no direct penetration of PA into the brain, we asked the question of whether circulating cytokines are responsible for the disruption of the brain endothelial barrier leading to BBB leakage. Brain

microvascular endothelial cells were exposed for 24 h to IL-1 β (2, 20 and 200 ng/mL) and the combination of IL-1 β and TNF- α (20 ng/mL). We elected those cytokines because they were highly expressed in the brain during PA pneumonia. Figure 7a shows the impact of cytokine exposure on barrier tightness. For IL-1 β , TER was significantly decreased by 50% (Fig. 7a, b), while the combination of cytokines caused a further decrease in TER (by 61%). In our previous work, brain microvascular endothelial cells showed a tight monolayer within 5 days, expressing ZO-1/claudin-5 and well-organized TJs, with a low permeability to small solutes [15]. Next, we studied the localization of the TJ proteins claudin-5 and ZO-1, and the AJ protein VE-cadherin upon IL-1 β treatment of brain endothelial cells. Endothelial cells under control conditions showed organized cell monolayers with clearly visible claudin-5, ZO-1 and VE-cadherin immunostaining. At the TER maximum (approximately 2.5 h after PA challenge). After IL-1 β treatment, claudin-5, ZO-1 and VE-cadherin immunostaining showed a diffused and discontinuous pattern with visible intercellular gaps and not fully outlining the circumference of each cell, illustrating severe damage to the integrity of the endothelial cell layer (Fig. 7c).

Discussion

This study shows that PA pneumonia causes BBB leakage, neuroinflammation, and behavior alteration (locomotor hyperactivity). The brain dysfunction occurred in the absence of direct infection of the cerebral vasculature or brain parenchyma; thus, we propose that the underlying mechanism involves an inflammatory response in the lung-brain axis linked by the circulation, characterized by an increased expression of

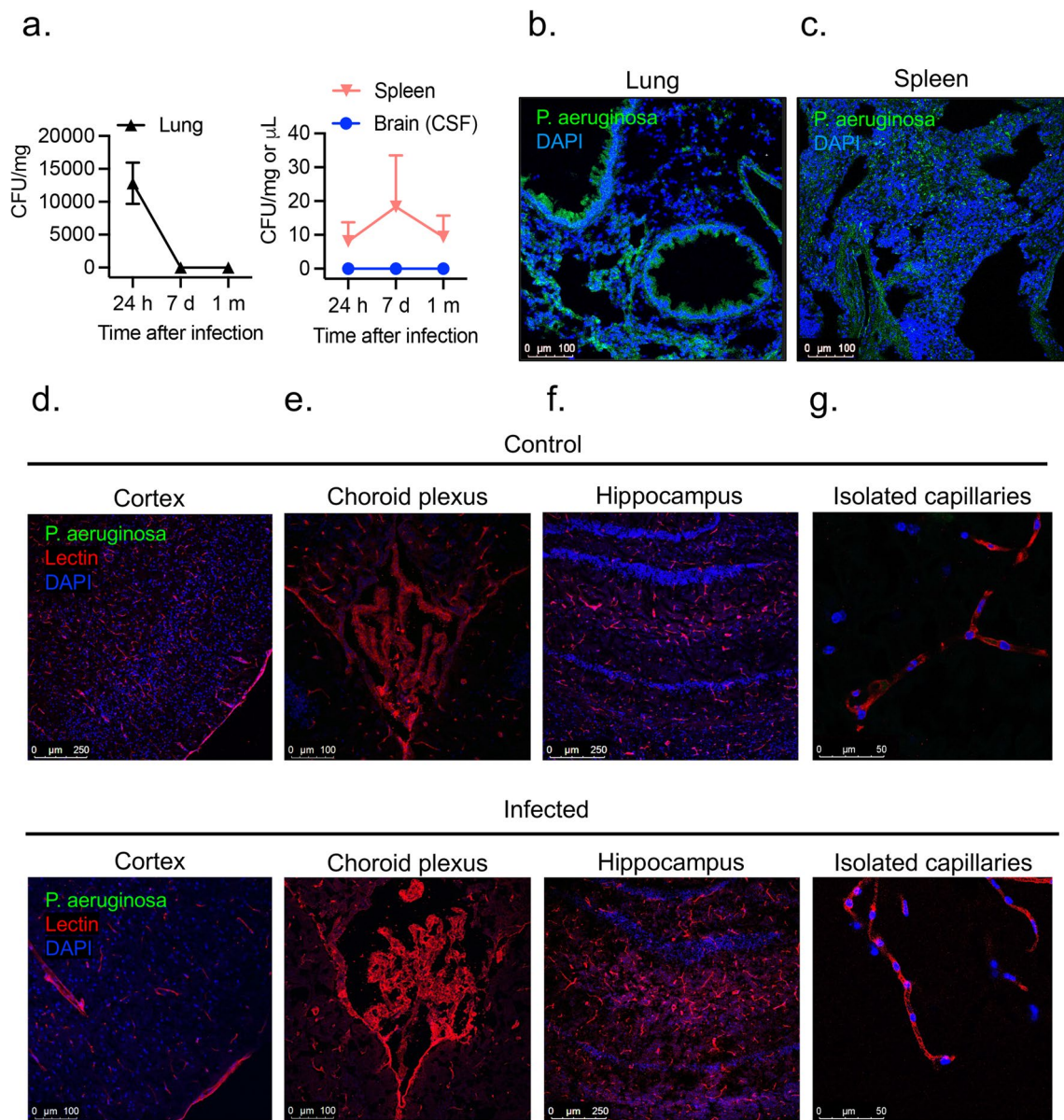


Fig. 4 PA load in peripheral organs and brain regions. **a** Bacterial growth in lung and spleen (CFUs per mg of tissue) and brain (in CSF; CFU per µL) obtained from infected animals (OD_{600} 0.3) and controls after intratracheal administration of PA at 24 h, 7-days and 1-month post-infection. **b** Representative confocal micrograph showing **(b)** lung and **(c)** spleen sections obtained from GFP-labelled PA infected animals at 24 h post-infection (OD_{600} 0.3) and controls. PA is labelled in green and nuclei (DAPI) in blue. **d–g** Representative confocal micrographs of **(d)** cortical sections, **(e)** choroid plexus **(f)** hippocampus and **(g)** isolated capillaries showing the lack of distribution of PA (GFP-labelled PA) in the brain of infected mice at 24 h post-infection and controls. Lectin (red) was used to label the blood vessels in tissue sections and claudin-5 or ZO-1 (red) to label isolated capillaries. DAPI (blue) was used to stain the nuclei

cytokines/chemokines and higher number of leukocytes in the blood and CNS. This is further supported by our data showing that cytokines exerted direct effects on cerebral microvascular endothelium to disrupt cell–cell junctions, reduce cell–cell adhesive barrier resistance, and increase BBB paracellular permeability.

PA is an opportunistic pathogen that can cause severe infectious disease in critically ill or immunocompromised individuals [26]. PA is responsible for a high percentage of hospital-acquired pneumonia in patients on medical devices, such as ventilators or catheters, as well as patients undergoing major surgeries [14, 27, 28].

Compared to the lungs and other organs, brain infection by PA is less common and limited to patients with head trauma or undergoing neurosurgical procedures, such as intracranial catheterization where PA gains direct access to the CNS [29, 30]. In this study, we used a clinically relevant mouse model of pneumonia via intratracheal delivery of PA. The animals received a moderate-to-high level of bacteria, which resulted in ~50% mortality at 7 days post-infection. This is in agreement with a previous study showing that administration of PA into murine lungs led to severe sepsis and death [31]. In our study, infected mice who survived for at least 24 h demonstrated typical symptoms of acute pneumonia, including low body temperature, high white blood cell and neutrophil counts, acidosis, and proteinemia. Histopathological observations indicated that intratracheal inoculation of PA triggered an inflammatory response in the lungs characterized by pulmonary barrier disruption and neutrophil infiltration. These changes coincided with pulmonary microvascular thrombosis, damaged endothelial lining, and capillary leakage. Infected animals showed high bacteria load in the lungs and blood stream. Together, these data support the validity of the PA-induced pneumonia model.

Interestingly, while PA positive cultures were obtained in the spleen, an organ remote from the lung, CSF cultures were negative. The absence of bacteria in the CNS is further supported by immunofluorescence and multiphoton microscopic evidence confirming that in our murine model of pneumonia, PA did not gain direct access to the brain. This finding is consistent with many other studies showing that *Pseudomonas meningitis* is often post-neurosurgical, rather than through direct penetration of PA into the CNS [27, 32, 33]. On the other hand, lung infection triggers a rapid and orchestrated activation of inflammatory cells and pathways leading to the production of an array of inflammatory mediators. These mediators can target tissues remote from the initial site of infection and cause multiple organ dysfunction. Within this context, the pathophysiological importance of the inflammatory response in the lung-brain axis to bacterial

infection has been well recognized. For example, recent studies have identified lung amyloids, tau proteins and endothelial glycocalyx fragments as bioproducts of acute lung infection can reach the CNS and affecting learning and memory [34–37]. However, the molecular mechanisms underlying lung-brain interactions remain poorly understood. Whether and how bacteria invasion into the lung affects the BBB structure and function have not been well studied. The present study provides novel evidence for the effects of bacterial lung infection on BBB permeability.

The maintenance of brain homeostasis is largely controlled by the BBB, a specialized neurovascular structure based on tightly sealed endothelial cells connected via cell–cell junctions (e.g., occludin, claudins, cadherins) surrounded by pericytes and astrocytic end-feet [38]. The BBB exhibits a very low permeability and is highly restrictive to the passage of cells, solutes, and pathogens, thus preventing neurotoxicity [39]. During pathological states such as injury or systemic inflammation, BBB breakdown leads to neuronal damage by allowing a plethora of circulating agents to enter the brain. Our data suggest that the BBB function is compromised during lung bacterial infection. *In vivo*, infected animals showed BBB leakage to tracers of different sizes, especially small molecules (NaF and 10-kDa), which indicates an increased paracellular permeability via compromised cell–cell junctions. We also observed a differential response of these junction molecules at different times. For example, while claudin-5 mRNA levels started to decline at early time points (within 24 h) post-infection, VE-cadherin decreased most significantly during the late stage (days) after infection. In addition, the mRNA expression level of occludin remained unaltered throughout the time course. There has been controversy regarding the role of occludin in determining TJ strength and BBB permeability property; while one study showed that occludin knockout mice present intact BBB [40], others have reported that changes in occludin expression induced by proinflammatory cytokines lead to changes in paracellular permeability [41, 42]. Further molecular analyses showed a

(See figure on next page.)

Fig. 5 Appearance of leukocytes in CNS during PA-induced lung infection. **a** White blood counts in control and PA-infected animals (OD₆₀₀ 0.3). Mann–Whitney test, $P=0.016$ vs. control (uninfected) group. **b** Neutrophil and monocyte counts in blood obtained from control and PA-infected mice (OD₆₀₀ 0.3) measured by ProCyte One hematology analyzer. Mann–Whitney test, $P=0.04$, $P=0.03$ vs. control (uninfected) group. **c** Flow cytometry analysis of brain tissue homogenates labeled with anti-CD45 and anti-CD11b antibodies with gating on CD45⁺ cells. Quantitative analyses of **(d)** infiltrated leukocytes and **(e)** microglia in control and PA infected mice. Mann–Whitney test, $P=0.03$ vs. control (uninfected) group. In all graphs, each point indicates data from an individual animal, bar graphs (columns and error bars) show mean \pm S.E.M. **f** Representative confocal images of infiltrated leukocytes (CD45⁺; green) in the brain from a control (left) and a PA-lung infected mouse (right). DAPI (nuclei; blue). **g** GFAP immunoblotting in brain homogenates from control and PA-infected (24 h after infection) mice, and quantification of GFAP protein abundance relative to β -actin loading control. Mann–Whitney test, $P=0.016$ vs. control (uninfected) group. **h** Representative confocal images of GFAP immunodetection (red), lectin-positive brain endothelial cells (green) and DAPI (nuclei; blue) in the brain of a control (left) and a PA-lung infected mouse (right). The inset in each main image (control and infected) represents a closer view of the indicated region at a higher magnification (right panels). In all graphs, each point indicates data from an individual animal, bar graphs (columns and error bars) show mean \pm S.E.M

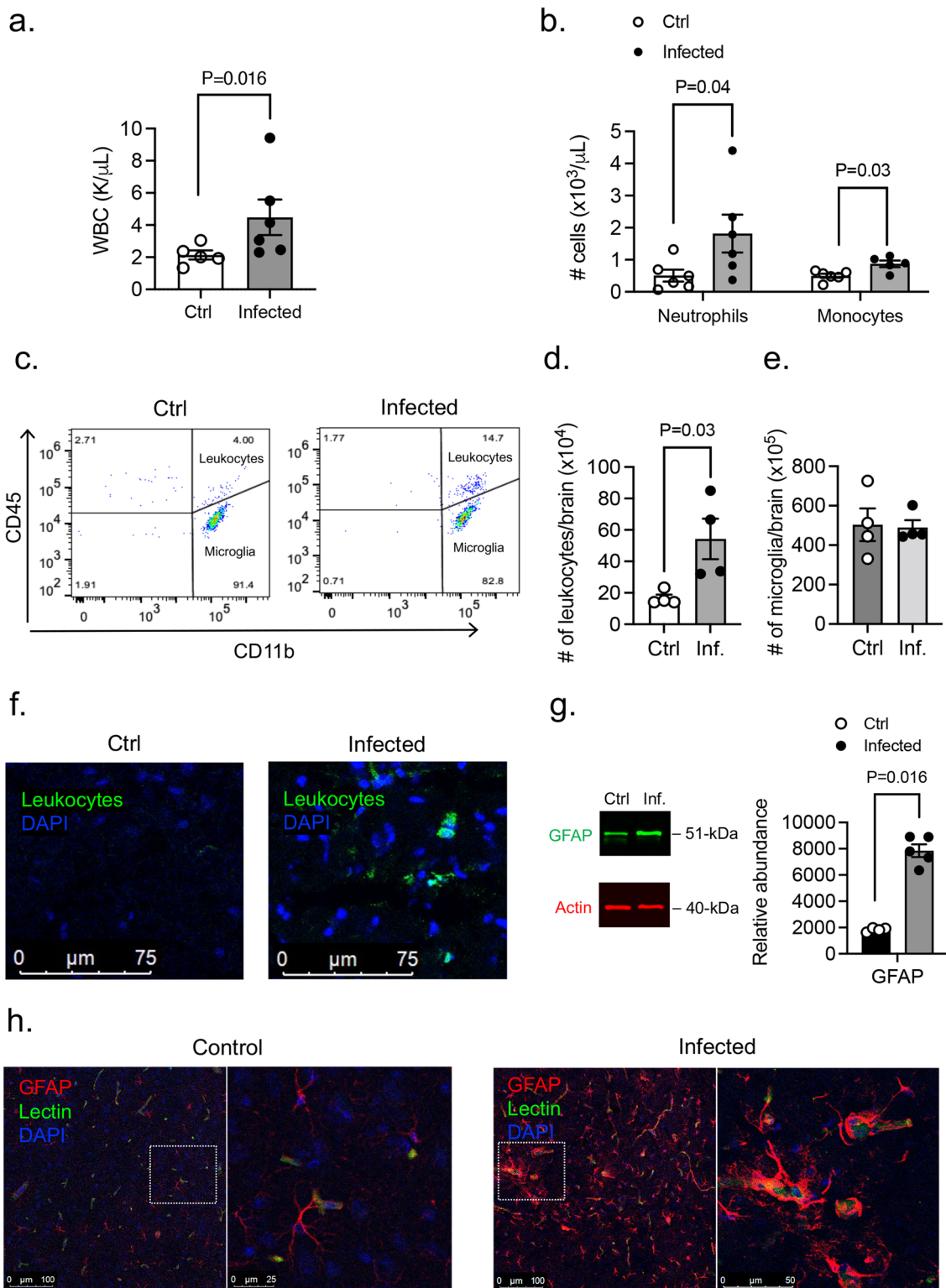


Fig. 5 (See legend on previous page.)

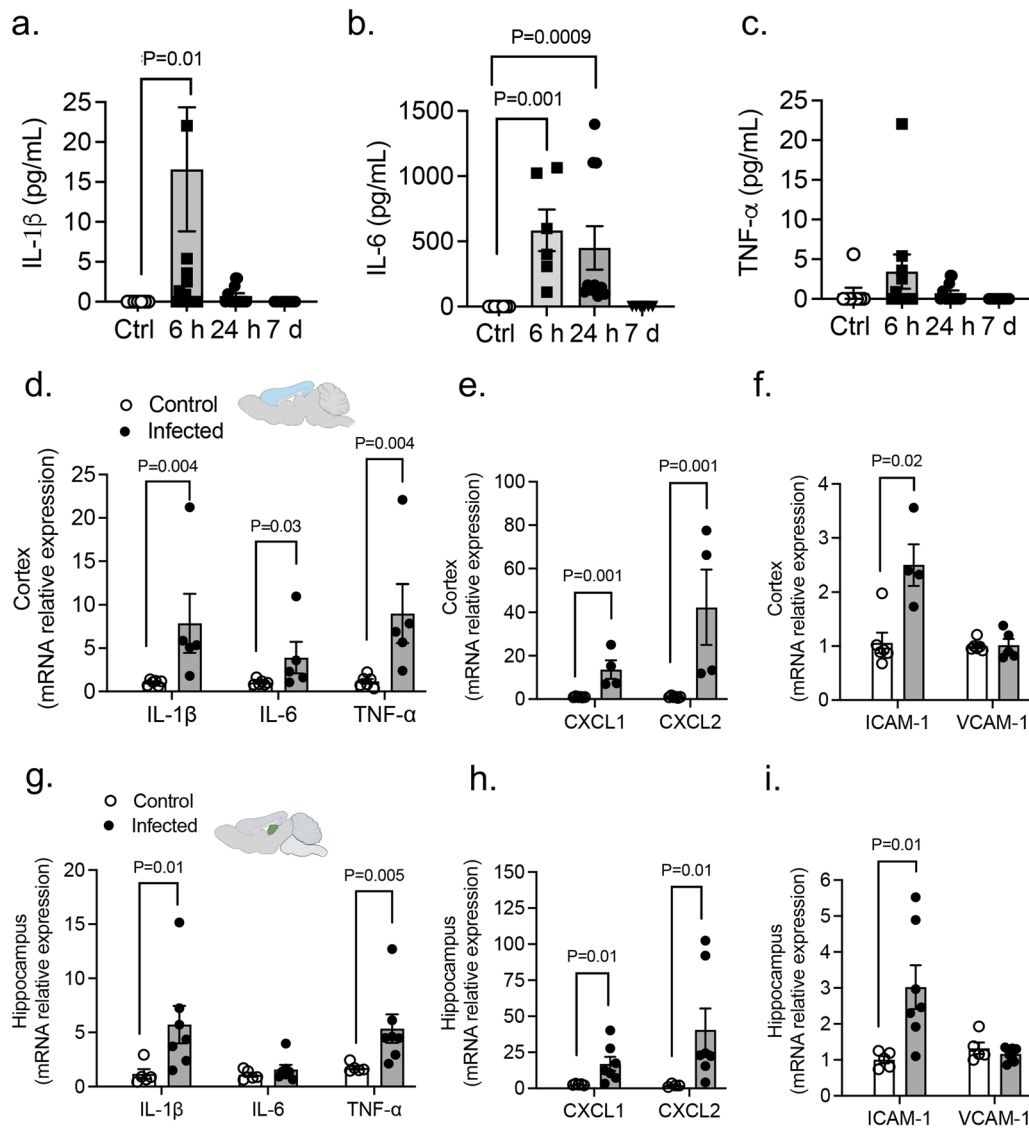


Fig. 6 PA lung infection causes systemic and neuroinflammation. **a–c** PA-induced plasma levels of IL-1 β , IL-6 and TNF- α at different time points after infection (OD_{600} 0.3) compared to uninfected controls. Kruskal–Wallis test, $P=0.01$, $P=0.001$ and $P=0.0009$ vs. control (uninfected) group. **d–f** mRNA expression levels of **(d)** cytokines (IL-1 β , IL-6 and TNF- α), **(e)** chemokines (CXCL1 and CXCL2) and **(f)** adhesion molecules (ICAM-1 and VCAM-1) in cortex from control and infected. Mann–Whitney test, $P=0.004$, $P=0.03$, $P=0.001$, $P=0.001$, $P=0.02$ vs. control (uninfected) group. **g–i** mRNA expression levels of **(g)** cytokines (IL-1 β , IL-6 and TNF- α), **(h)** chemokines (CXCL1 and CXCL2) and **(i)** adhesion molecules (ICAM-1 and VCAM-1) in hippocampus from control and infected mice. Mann–Whitney test, $P=0.01$, $P=0.005$ vs. control (uninfected) group. In all graphs, each point indicates data from an individual animal bar graphs (columns and error bars) show mean \pm S.E.M

significant decrease in occludin and VE-cadherin protein expression levels at 24 h post-infection compared to controls.

As the endothelial barrier is in contact with circulating mediators whose levels vary under different pathophysiological conditions [43], we sought to characterize the direct effects of proinflammatory cytokines on BBB junction structure and function. Our model showed high levels of proinflammatory cytokines in the plasma

of infected animals, supporting that systemic inflammation is part of disease progression following PA lung infection. In particular, the plasma levels of IL-1 β and IL-6 and TNF- α were significantly elevated. Importantly, we also detected an increased expression of multiple cytokines and chemokines in the brain, with IL-1 β and TNF- α as the most significantly elevated in both cortex and hippocampus regions. Therefore, we selected these cytokines for testing their effects on brain microvascular

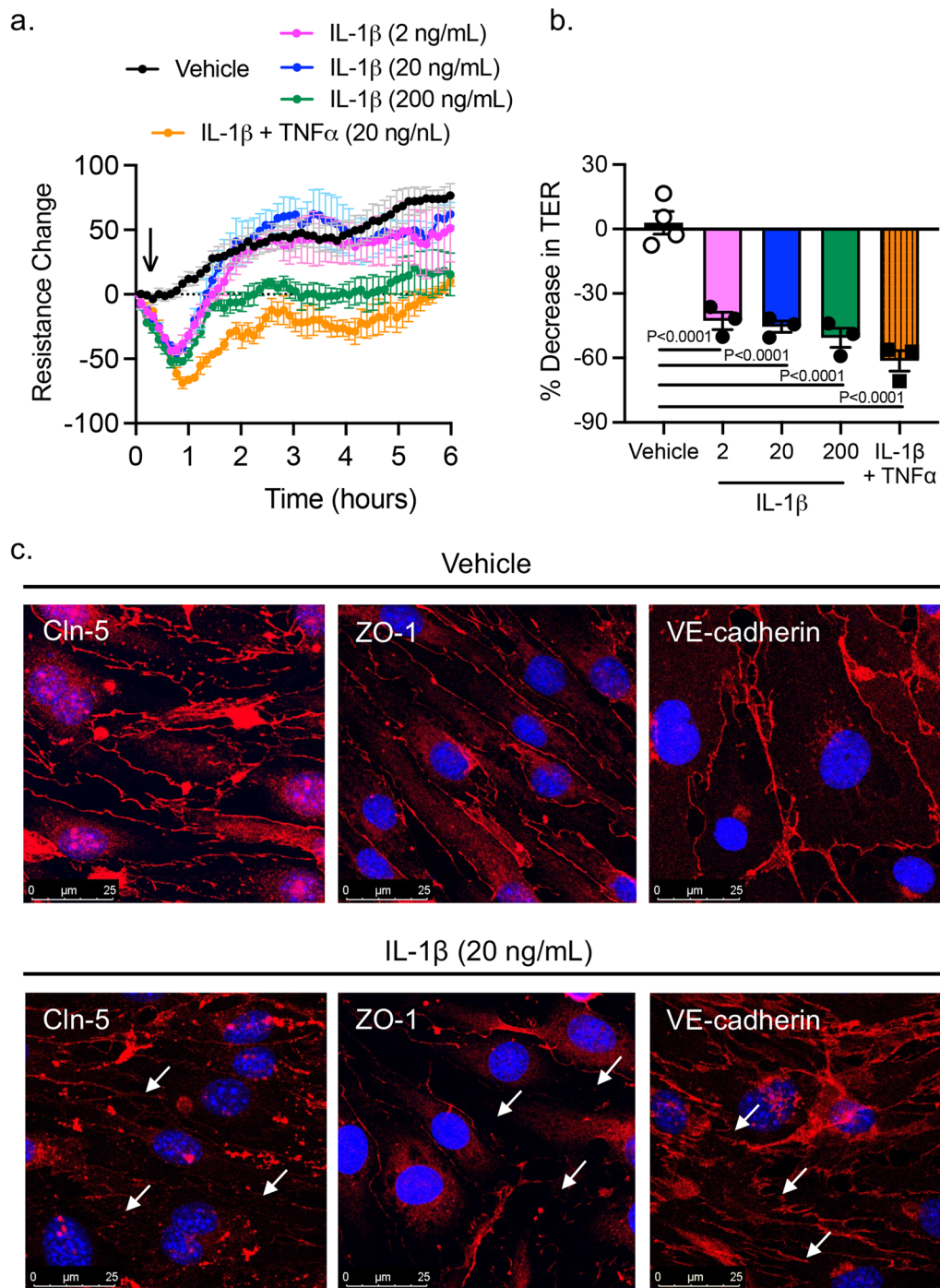


Fig. 7 Effect of proinflammatory cytokines on brain microvascular endothelial barrier function. **a** TER measurements across confluent monolayers of mouse brain microvascular endothelial cells treated with IL-1 β (2–200 ng/mL) and IL-1 β +TNF- α (20 ng/mL each). The data were represented as resistance change. Mean \pm S.E.M., $n=3$. Arrow indicates when cytokines were added. **b** Summary data showing TER changes in brain microvascular endothelial cells treated with IL-1 β and IL-1 β +TNF- α . Kruskal–Wallis test with Dunn’s multiple comparisons test, $P < 0.0001$, IL-1 β (2–200 ng/mL) vs. control (vehicle) group; $P < 0.0001$, IL-1 β +TNF- α (20 ng/mL each) vs. control (vehicle). **c** Immunocytochemical analysis of claudin-5, VE-cadherin and ZO-1 (red) on brain microvascular endothelial cells under control conditions (vehicle) and after IL-1 β (20 ng/mL) treatment in vitro. Nuclei was stained with DAPI. White arrows indicate TJ disorganization

endothelial junctions in vitro. Our barrier resistance (ECIS) data showed that IL-1 β induced a dose-dependent reduction in TER, indicator of cell–cell junction function, and this effect was augmented during combined treatment with IL-1 β and TNF- α . Structurally, compared to control brain endothelial monolayers showing clearly defined TJs with continuous lining of claudin-5, ZO-1 and VE-cadherin at cell–cell contacts, IL-1 β -treated endothelial cells showed discontinuous junction lining with VE-cadherin stained in a finger-like pattern and claudin-5 and ZO-1 showing intercellular gaps. These results reinforce the cytokines' ability to disrupt the BBB integrity. Indeed, previous studies have demonstrated a correlation between in vivo administration of pro-inflammatory cytokines and BBB leakage [40, 44]. The ability of cytokines to open the paracellular pathway of endothelial barrier has been attributed to endothelial cytoskeleton reorganization [25] and/or downregulation of junction protein expression [23, 41, 45–51].

The microvascular leakage and BBB hyperpermeability observed in PA-infected animals were associated with neuroinflammation, evidenced by immune cell recruitment and high expression of proinflammatory cytokines, chemokines and adhesion molecules and reactive astrogliosis in the brain of mice with pneumonia. It is known that lung infection or injury is associated with various neurological complications, from altered memory to cognitive decline [52–55]. In our model, even in the absence of direct penetration of PA into the brain, infected mice developed anxiety-like behaviors, which might result from cerebral microvascular dysfunction, BBB leakage, and systemic/local production of cytotoxic cytokines like IL-1 β [56–58] and TNF- α [48, 59] as previously documented.

Conclusions

The present study demonstrates that bacterial infection in the lungs causes neuroinflammation, cerebral microvascular leakage and increased BBB paracellular permeability; the underlying mechanisms involve cytokine-induced brain endothelial cell–cell adhesive barrier dysfunction and downregulation of cell–cell junctions. These data provide novel evidence supporting the mechanistic linkage between the lung and brain as part of an orchestrated host immune response to bacterial infection. In addition, our study is unique because we have developed and validated a mouse model of pneumonia that may prove useful in studying the brain sequelae of infectious diseases originated from non-CNS organs.

Abbreviations

AJ	Adherens junction
BBB	Blood–brain barrier

CFUs	Colony forming units
CNS	Central nervous system
ELISA	Enzyme-linked immunosorbent assay
GFP	Green fluorescent protein
H&E	Hematoxylin and Eosin
IL	Interleukin
NaFl	Sodium fluorescein
OD	Optical density
PA	<i>Pseudomonas aeruginosa</i>
PBS	Phosphate buffer saline
PFA	Paraformaldehyde
TER	Transendothelial electrical resistance
TJs	Tight junctions
TNF	Tumor necrosis factor

Supplementary Information

The online version contains supplementary material available at <https://doi.org/10.1186/s12974-023-02817-7>.

Additional file 1: Figure S1. Representative flow cytometry plots illustrate the gating strategy used for this experimental series: single cell population was gated based on forward-scatter characteristics, Zombie viability dye was used to exclude dead cells, and CD45 and CD11b staining were used to identify myeloid leukocytes and microglia subpopulation of cells.

Additional file 2: Figure S2. Effect of PA on mouse survival, body temperature and biochemistry parameters. Survival rates of mice treated with PA at OD₆₀₀ 0.3 and 0.6. Body temperature obtained by measuring the rectal temperature after PA infection. Blood pH values obtained from control and PA-infected mice at 4 h and 24 h after infection measured with iSTAT. Total protein concentration in blood measured in controls and 24-h after PA infection.

Additional file 3: Figure S3. Full scans of all Western blots used for quantification in main figures. Western blots of VE-cadherin, occludin and claudin-5 in cerebral cortex homogenates from controls and infected mice at 24 h post-infection. Western blots of GFAP in cerebral cortex homogenates from controls and infected mice at 24 h post-infection. Dotted boxes indicate lanes presented as representative blots in the respective main figures.

Additional file 4: Video 1. Localization of PA in lung parenchyma in PA-infected mice. Movie showing 3D projections of GFP-labelled PA and its spatial relation to the vasculature labelled with Evans blue.

Additional file 5: Video 2. Lung parenchyma in control uninfected mice. Movie showing 3D projections lung parenchyma in uninfected mice and its vasculature labelled with Evans blue.

Additional file 6: Video 3. Brain vasculature in PA-infected mice. Movie showing 3D projections of brain cortex and its vasculature labelled with Evans blue in GFP-labelled PA-infected mice.

Additional file 7: Video 4. Brain vasculature in control uninfected mice. Movie showing 3D projections of brain cortex and its vasculature labelled with Evans blue in control uninfected mice.

Acknowledgements

No applicable.

Author contributions

NV performed experiments, analyzed data and wrote the manuscript. YM and SS performed flow cytometry experiments. SAG performed experiments, PA cultures and helped with data analysis. AJA and KRIN helped with neurological testing experiments. XY helped with tissue/blood collection. SYY conceptualize the study, edited and revised the manuscript and provided support through all levels of development. All authors read and approved the final version of the manuscript.

Funding

This work was supported by the National Institutes of Health Grants HL150732 and GM142110 (to SYY).

Availability of data and materials

The datasets used and/or analyzed during the current study are available from the corresponding author on reasonable request.

Declarations

Ethics approval and consent to participate

Not applicable.

Consent for publication

Not applicable.

Competing interests

The authors declare that they have no competing interests.

Author details

¹Department of Molecular Pharmacology and Physiology, Morsani College of Medicine, University of South Florida, Tampa, FL, USA. ²Department of Surgery, Morsani College of Medicine, University of South Florida, Tampa, FL, USA.

Received: 24 January 2023 Accepted: 23 May 2023

Published online: 27 May 2023

References

- McManus RM, Higgins SC, Mills KH, Lynch MA. Respiratory infection promotes T cell infiltration and amyloid-beta deposition in APP/PS1 mice. *Neurobiol Aging*. 2014;35(1):109–21.
- Rubin K, Glazer S. The pertussis hypothesis: Bordetella pertussis colonization in the pathogenesis of Alzheimer's disease. *Immunobiology*. 2017;222(2):228–40.
- Maheshwari P, Eslick GD. Bacterial infection and Alzheimer's disease: a meta-analysis. *J Alzheimers Dis*. 2015;43(3):957–66.
- Janssens JP, Krause KH. Pneumonia in the very old. *Lancet Infect Dis*. 2004;4(2):112–24.
- Gofton TE, Young GB. Sepsis-associated encephalopathy. *Nat Rev Neurol*. 2012;8(10):557–66.
- Beutz MA, Abraham E. Community-acquired pneumonia and sepsis. *Clin Chest Med*. 2005;26(1):19–28.
- Ranzani OT, Prina E, Menendez R, Ceccato A, Cilloniz C, Mendez R, et al. New sepsis definition (Sepsis-3) and community-acquired pneumonia mortality. A validation and clinical decision-making study. *Am J Respir Crit Care Med*. 2017;196(10):1287–97.
- Rello J, Perez A. Precision medicine for the treatment of severe pneumonia in intensive care. *Expert Rev Respir Med*. 2016;10(3):297–316.
- Ren C, Yao RQ, Zhang H, Feng YW, Yao YM. Sepsis-associated encephalopathy: a vicious cycle of immunosuppression. *J Neuroinflammation*. 2020;17(1):14.
- Annane D, Sharshar T. Cognitive decline after sepsis. *Lancet Respir Med*. 2015;3(1):61–9.
- Mazeraud A, Pascal Q, Verdonk F, Heming N, Chretien F, Sharshar T. Neuroanatomy and physiology of brain dysfunction in sepsis. *Clin Chest Med*. 2016;37(2):333–45.
- Erkkinen MG, Berkowitz AL. A clinical approach to diagnosing encephalopathy. *Am J Med*. 2019;132(10):1142–7.
- Dando SJ, Mackay-Sim A, Norton R, Currie BJ, St John JA, Ekberg JA, et al. Pathogens penetrating the central nervous system: infection pathways and the cellular and molecular mechanisms of invasion. *Clin Microbiol Rev*. 2014;27(4):691–726.
- Flanders SA, Collard HR, Saint S. Nosocomial pneumonia: state of the science. *Am J Infect Control*. 2006;34(2):84–93.
- Villalba N, Baby S, Cha BJ, Yuan SY. Site-specific opening of the blood-brain barrier by extracellular histones. *J Neuroinflammation*. 2020;17(1):281.
- Bustin SA, Benes V, Garson JA, Hellemans J, Huggett J, Kubista M, et al. The MIQE guidelines: minimum information for publication of quantitative real-time PCR experiments. *Clin Chem*. 2009;55(4):611–22.
- Ma Y, Yang X, Villalba N, Chatterjee V, Reynolds A, Spence S, et al. Circulating lymphocyte trafficking to the bone marrow contributes to lymphopenia in myocardial infarction. *Am J Physiol Heart Circ Physiol*. 2022;322(4):H622–35.
- Beard RS Jr, Hoettels BA, Meegan JE, Wertz TS, Cha BJ, Yang X, et al. AKT2 maintains brain endothelial claudin-5 expression and selective activation of IR/AKT2/FOXO1-signaling reverses barrier dysfunction. *J Cereb Blood Flow Metab*. 2020;40(2):374–91.
- Lee YK, Uchida H, Smith H, Ito A, Sanchez T. The isolation and molecular characterization of cerebral microvessels. *Nat Protoc*. 2019;14(11):3059–81.
- Belzung C, Griebel G. Measuring normal and pathological anxiety-like behaviour in mice: a review. *Behav Brain Res*. 2001;125(1–2):141–9.
- Pan J, Wan J. Methodological comparison of FACS and MACS isolation of enriched microglia and astrocytes from mouse brain. *J Immunol Methods*. 2020;486: 112834.
- Capaldo CT, Nusrat A. Cytokine regulation of tight junctions. *Biochim Biophys Acta*. 2009;1788(4):864–71.
- Rigor RR, Beard RS Jr, Litovka OP, Yuan SY. Interleukin-1beta-induced barrier dysfunction is signaled through PKC-theta in human brain microvascular endothelium. *Am J Physiol Cell Physiol*. 2012;302(10):C1513–22.
- Beard RS Jr, Haines RJ, Wu KY, Reynolds JJ, Davis SM, Elliott JE, et al. Non-muscle Mlck is required for beta-catenin- and FoxO1-dependent downregulation of Cldn5 in IL-1beta-mediated barrier dysfunction in brain endothelial cells. *J Cell Sci*. 2014;127(Pt 8):1840–53.
- de Vries HE, Blom-Roosemalen MC, van Oosten M, de Boer AG, van Berkel TJ, Breimer DD, et al. The influence of cytokines on the integrity of the blood-brain barrier in vitro. *J Neuroimmunol*. 1996;64(1):37–43.
- Rello J, Rue M, Jubert P, Muses G, Sonora R, Valles J, et al. Survival in patients with nosocomial pneumonia: impact of the severity of illness and the etiologic agent. *Crit Care Med*. 1997;25(11):1862–7.
- Rodriguez-Lucas C, Fernandez J, Martinez-Sela M, Alvarez-Vega M, Moran N, Garcia A, et al. *Pseudomonas aeruginosa* nosocomial meningitis in neurosurgical patients with intraventricular catheters: therapeutic approach and review of the literature. *Enferm Infecc Microbiol Clin (Engl Ed)*. 2020;38(2):54–8.
- Huang CR, Lu CH, Chuang YC, Tsai NW, Chang CC, Chen SF, et al. Adult *Pseudomonas aeruginosa* meningitis: high incidence of underlying medical and/or postneurosurgical conditions and high mortality rate. *Jpn J Infect Dis*. 2007;60(6):397–9.
- Chuang YC, Chang WN, Lu CH, Wu HS, Chang HW. *Pseudomonas aeruginosa* central nervous system infections: analysis of clinical features of 16 adult patients. *Zhonghua Yi Xue Za Zhi (Taipei)*. 1999;62(5):300–7.
- Boque MC, Bodi M, Rello J. Trauma, head injury, and neurosurgery infections. *Semin Respir Infect*. 2000;15(4):280–6.
- Bragonzi A. Murine models of acute and chronic lung infection with cystic fibrosis pathogens. *Int J Med Microbiol*. 2010;300(8):584–93.
- Gallagher C, Norman J, Singh A, Sanderson F. Community-acquired *Pseudomonas aeruginosa* meningitis. *BMJ Case Rep*. 2017;2017.
- Batlle Almodovar Mdel C, Dickinson F, Perez Monras M, Tamargo Martinez I, Similis A. Bacterial meningitis and *Pseudomonas aeruginosa*: apropos of a case. *Rev Cubana Med Trop*. 2005;57(3):230–2.
- Balczon R, Lin MT, Lee JY, Abbasi A, Renema P, Voth SB, et al. Pneumonia initiates a tauopathy. *FASEB J*. 2021;35(9): e21807.
- Scott AM, Jager AC, Gwin M, Voth S, Balczon R, Stevens T, et al. Pneumonia-induced endothelial amyloids reduce dendritic spine density in brain neurons. *Sci Rep*. 2020;10(1):9327.
- Balczon R, Pittet JF, Wagener BM, Moser SA, Voth S, Vorhees CV, et al. Infection-induced endothelial amyloids impair memory. *FASEB J*. 2019;33(9):10300–14.
- Hippensteel JA, Anderson BJ, Orfila JE, McMurtry SA, Dietz RM, Su G, et al. Circulating heparan sulfate fragments mediate septic cognitive dysfunction. *J Clin Invest*. 2019;129(4):1779–84.
- Sweeney MD, Zhao Z, Montagne A, Nelson AR, Zlokovic BV. Blood-brain barrier: from physiology to disease and back. *Physiol Rev*. 2019;99(1):21–78.
- Pardridge WM. Drug transport across the blood-brain barrier. *J Cereb Blood Flow Metab*. 2012;32(11):1959–72.

40. Saitou M, Furuse M, Sasaki H, Schulzke JD, Fromm M, Takano H, et al. Complex phenotype of mice lacking occludin, a component of tight junction strands. *Mol Biol Cell*. 2000;11(12):4131–42.
41. Rochfort KD, Collins LE, Murphy RP, Cummins PM. Downregulation of blood-brain barrier phenotype by proinflammatory cytokines involves NADPH oxidase-dependent ROS generation: consequences for interendothelial adherens and tight junctions. *PLoS ONE*. 2014;9(7): e101815.
42. Van Itallie CM, Fanning AS, Holmes J, Anderson JM. Occludin is required for cytokine-induced regulation of tight junction barriers. *J Cell Sci*. 2010;123(Pt 16):2844–52.
43. Tunkel AR, Rosser SW, Hansen EJ, Scheld WM. Blood-brain barrier alterations in bacterial meningitis: development of an in vitro model and observations on the effects of lipopolysaccharide. *In Vitro Cell Dev Biol*. 1991;27A(2):113–20.
44. Saija A, Princi P, Lanza M, Scalese M, Aramnejad E, De Sarro A. Systemic cytokine administration can affect blood-brain barrier permeability in the rat. *Life Sci*. 1995;56(10):775–84.
45. Rochfort KD, Collins LE, McLoughlin A, Cummins PM. Tumour necrosis factor- α -mediated disruption of cerebrovascular endothelial barrier integrity in vitro involves the production of proinflammatory interleukin-6. *J Neurochem*. 2016;136(3):564–72.
46. Rochfort KD, Cummins PM. Cytokine-mediated dysregulation of zonula occludens-1 properties in human brain microvascular endothelium. *Microvasc Res*. 2015;100:48–53.
47. Rochfort KD, Cummins PM. The blood-brain barrier endothelium: a target for pro-inflammatory cytokines. *Biochem Soc Trans*. 2015;43(4):702–6.
48. Versele R, Sevin E, Gosselet F, Fenart L, Candela P. TNF- α and IL-1 β modulate blood-brain barrier permeability and decrease amyloid- β peptide efflux in a human blood-brain barrier Model. *Int J Mol Sci*. 2022;23(18):10235.
49. Peditakis I, Kodella KR, Manatakis DV, Le CY, Barthakur S, Sorets A, et al. A microengineered Brain-Chip to model neuroinflammation in humans. *iScience*. 2022;25(8):104813.
50. Haines RJ, Beard RS Jr, Wu MH. Protein tyrosine kinase 6 mediates TNF α -induced endothelial barrier dysfunction. *Biochem Biophys Res Commun*. 2015;456(1):190–6.
51. Haines RJ, Beard RS Jr, Chen L, Eitnier RA, Wu MH. Interleukin-1 β mediates beta-catenin-driven downregulation of claudin-3 and barrier dysfunction in Caco2 cells. *Dig Dis Sci*. 2016;61(8):2252–61.
52. Quilez ME, Fuster G, Villar J, Flores C, Marti-Sistac O, Blanch L, et al. Injurious mechanical ventilation affects neuronal activation in ventilated rats. *Crit Care*. 2011;15(3):R124.
53. Gonzalez-Lopez A, Lopez-Alonso I, Aguirre A, Amado-Rodriguez L, Batalla-Solis E, Astudillo A, et al. Mechanical ventilation triggers hippocampal apoptosis by vagal and dopaminergic pathways. *Am J Respir Crit Care Med*. 2013;188(6):693–702.
54. Pelosi P, Ferguson ND, Frutos-Vivar F, Anzueto A, Putensen C, Raymondos K, et al. Management and outcome of mechanically ventilated neurologic patients. *Crit Care Med*. 2011;39(6):1482–92.
55. Huang HY, Huang CY, Li LF. Prolonged Mechanical Ventilation: Outcomes and Management. *J Clin Med*. 2022;11(9):2451.
56. Michael BD, Griffiths MJ, Granerod J, Brown D, Keir G, Wnek M, et al. The interleukin-1 balance during encephalitis is associated with clinical severity, blood-brain barrier permeability, neuroimaging changes, and disease outcome. *J Infect Dis*. 2016;213(10):1651–60.
57. Labus J, Hackel S, Lucka L, Danker K. Interleukin-1 β induces an inflammatory response and the breakdown of the endothelial cell layer in an improved human THBMEC-based in vitro blood-brain barrier model. *J Neurosci Methods*. 2014;228:35–45.
58. Melnikov PA, Valikhov MP, Kuznetsov II, Grinenko NF, Sukhinich KK, Simbirtsev AS, et al. Analysis of the effect of IL-1 β on blood-brain barrier permeability in m6 glioma mouse model using intravital microscopy. *Bull Exp Biol Med*. 2019;168(1):118–24.
59. Nishioku T, Matsumoto J, Dohgu S, Sumi N, Miyao K, Takata F, et al. Tumor necrosis factor- α mediates the blood-brain barrier dysfunction induced by activated microglia in mouse brain microvascular endothelial cells. *J Pharmacol Sci*. 2010;112(2):251–4.

Publisher's Note

Springer Nature remains neutral with regard to jurisdictional claims in published maps and institutional affiliations.

Ready to submit your research? Choose BMC and benefit from:

- fast, convenient online submission
- thorough peer review by experienced researchers in your field
- rapid publication on acceptance
- support for research data, including large and complex data types
- gold Open Access which fosters wider collaboration and increased citations
- maximum visibility for your research: over 100M website views per year

At BMC, research is always in progress.

Learn more biomedcentral.com/submissions

